Materials' effects on the elevated and room temperature performance of C/LiMn$_2$O$_4$ Li-ion batteries

G.G. Amatucci [a,*], C.N. Schmutz [a], A. Blyr [b], C. Sigala [b], A.S. Gozdz [a], D. Larcher [b], J.M. Tarascon [b]

[a] Bellcore, Red Bank, NJ 07701, USA
[b] Université de Picardie Jules Verne, Amiens, 80000 France

Abstract

Li-ion rechargeable batteries based on LiMn$_2$O$_4$ suffer from relatively poor storage and cycling performance at elevated temperatures. In order to address this issue, a structural and electrochemical study of LiMn$_2$O$_4$-based systems at room and elevated temperatures were undertaken. Some of the spinel material characteristics such as morphology, defects, surface area, structural instability, single- versus two-phase lithium-insertion processes, cation and oxygen stoichiometry, and manganese solubility were investigated. We found that the sample surface area, which also influences the manganese dissolution and electrolyte oxidation, is one of the most critical parameters in controlling the rate of irreversible self-discharge, with the lowest irreversible self-discharge being observed for samples with the lowest surface area. These results are discussed in terms of active surface centers and the possibility of surface treatments to rectify this problem. The elevated temperature storage and room temperature cycling performance was found to be the best for those Li$_x$Mn$_2$O$_{4 + \delta}$ samples having a low surface area (0.5–1 m^2/g), Li in excess ($x > 1.00$), show no evidence of Jahn–Teller distortion down to -50 °C, and for which the Li-extraction mechanism occurs over a single-phase reaction at room temperature. © 1977 Published by Elsevier Science S.A.

1. Introduction

Li-ion technology is presently enjoying a great commercial success. Almost all commercial Li-ion cells are presently based on the carbon/liquid electrolyte/LiCoO$_2$ redox system in which the negative carbon electrode can be either graphite or coke [1,2]. However, while operating well as a positive intercalation electrode in such batteries, LiCoO$_2$ is expensive due to the natural rarity of cobalt in nature. To sustain the increasing demand for the Li-ion battery by the portable electronics market and the expected demand by the electric vehicle market, alternative cathode materials able to reversibly insert Li at high voltages must be studied. While the intensive search for such new materials continues, we have to pursue a parallel effort to optimize known alternatives to LiCoO$_2$. Among the candidates are the LiNiO$_2$-layered oxide [3] and, more specifically, the three-dimensional spinel LiMn$_2$O$_4$ [4–7] which offers cost and environmental advantages.

By recognition of the strong influence material aspects (processing conditions, cationic and oxygen stoichiometry, particle morphology) have on the resultant electrochemical performance of LiMn$_2$O$_4$, Bellcore's researchers [8–13] have demonstrated the practical feasibility of LiMn$_2$O$_4$/Li-ion cells. Along with parallel and subsequent research efforts by others, e.g. Gummow et al. [14], these researchers have eliminated one of the main obstacles to the wide use of the spinel LiMn$_2$O$_4$ in Li-ion cells, namely, the poor cycle life (e.g. rapid capacity fading) at room temperature [11–13]. Presently, both C/electrolyte/LiCoO$_2$ and C/electrolyte/LiMn$_2$O$_4$ cells perform identically at room temperature in terms of cycle-life and power rate. While the potential advantage of LiMn$_2$O$_4$ for large-scale manufacturing is well recognized by the battery community, and in spite of the recent advances in the understanding of LiMn$_2$O$_4$ materials and their electrochemical aspects, battery manufacturers are still hesitant to use LiMn$_2$O$_4$ in place of LiCoO$_2$ in their products.

Another important concern for the wide use of the spinel as the positive electrode has now become the large capacity loss observed during storage at elevated temperatures, such as 55 °C, of charged C/electrolyte/LiMn$_2$O$_4$ Li-ion cells

* Corresponding author. Tel.: +1-908-758-33 58; Fax: +1-908-758-43 78.

(e.g. large irreversible self-discharge). Depending on the battery technology, this capacity loss during storage can be totally or partially reversible. For instance, with aqueous systems such as Ni–Cd or Ni–MeH, self-discharge as large as 60% per month have been measured. For such systems, however, the self-discharge mechanism which involves water electrolysis is mainly reversible through a recombination process (e.g. self-healing mechanism). This is in total contrast with the Li-ion technology, for which the self-discharge was ascribed to partially irreversible local redox processes occurring simultaneously at the negative and positive electrode interfaces [15]. Each local process involves a reversible reaction (Li insertion) and an irreversible reaction (electrolyte breakdown) with the main result being an irreversible capacity loss. As the electrolyte oxidation is kinetically governed, local redox reactions are accelerated with increasing cell-operating temperatures, resulting in poor storage performance at elevated temperature (e.g., large self-discharge). Because of the absence of self-healing mechanism in the Li-ion technology, this irreversibility is cumulative over time, so that 50% permanent capacity loss can be measured on non-optimized cells that are stored for two months at 55 °C. Reducing the self-discharge both at room temperature and 55 °C is then essential to the success of the spinel based Li-ion technology.

Tarascon and coworkers [16,17] have previously described the electrolyte breakdown as the result of a catalytically induced process with the spinel phase playing the role of a catalytic agent and thereby stressed the importance of controlling the surface area of powdered $LiMn_2O_4$ specimens. Based on this finding, electrochemically optimized $LiMn_2O_4$ powders for room-temperature applications were reported. We have been pursuing such studies to finely tune the synthesis of $LiMn_2O_4$ to obtain improved elevated temperature performance. More specifically, we investigated which of the following parameters: morphology, surface area, structural instability, cation/anion non-stoichiometry, manganese solubility, which in turn are closely related to sample processing, are governing the catalytic activity of $LiMn_2O_4$ specimens, and thereby the amplitude of the irreversible capacity loss on storage in the charged state at 55 °C. The surface area of the sample turns out to be the most important parameter, with the observation of the largest surface area having the largest 55 °C self-discharge. Being able to control this parameter C/electrolyte/$LiMn_2O_4$ Li-ion cells with 55 °C storage loss capacity similar to commercial C/electrolyte/$LiCoO_2$ Li-ion cells were able to be achieved.

This paper is organized as follows: an experimental section is followed by a detailed structural and electrochemical study of two series of samples: $Li_{1+x}Mn_{2-x}O_4$ and $Li_{1.05}Mn_{1.95}O_4$, for which x and the annealing conditions are the separated variables, respectively. Cycle life and storage data at 55 °C are then reported as a segue to sections discussing the λ-MnO_2 decomposition, single-phase versus biphase intercalation/de-intercalation process and, the importance of surface

area and sample morphology. In closing, a discussion section will try to reconcile all the experimental data.

It should be noted that throughout the text, the general notation for the stoichiometry of the spinel will be indicated as $Li_xMn_2O_{4+\delta}$ as a reminder that, as x exceeds 1, the average oxidation state of manganese increases. This will be done for ease of figure presentation. For spinels with Li content exceeding 1 there exists an Li substitution onto the octahedral sites which can be represented by the more traditional notation $(Li)_{tet}[Li_xMn_{2-x}]_{oct}O_4$.

2. Experimental

$Li_xMn_2O_{4+\delta}$ samples (with x ranging from 0.925 to 1.1 in 0.025 steps) in the powder form were prepared by mixing stoichiometric amounts of Li salts and Mn-based oxides. The precursor materials were Li_2CO_3 and EMD-MnO_2 (electrochemical manganese dioxide). Unless otherwise specified, the materials were prepared as reported in Refs. [11–13] with a sequence of anneals at 800 °C and intermittent grindings followed by a final slow cooling of the samples.

A large batch of $Li_{1.05}Mn_{1.95}O_4$ powder was also prepared as above, divided prior to the last step into six identical samples that were heated at 800, 860, 915, 965, 1015 and 1065 °C for 5 h, respectively, maintained at these temperatures for 12 h and cooled in 5 h to room temperature. These six samples were then reannealed at 800 °C and slowly cooled to 500 °C (this series denoted 'HT' in a sequential manner), followed by furnace cooling to room temperature.

The resulting samples were characterized by X-ray diffraction (XRD) using a Scintag PAD V X-ray diffractometer using Cu $K\alpha$ radiation. The structural decomposition of the delithiated λ-MnO_2 samples in air as a function of temperature was followed by a high-temperature Guinier–Lenne camera through continuous film recording. Structural phase changes occurring during the de-insertion/insertion of Li within the spinel phase were followed by means of a newly developed in situ electrochemical cell which can be used to cell voltages beyond 5 V [18]. This cell, was mounted on the Scintag diffractometer, connected to a HP computer-controlled current source and charged to 5.2 V. Data points were collected every 0.01 V during a charge at a rate of C/30. In situ X-ray measurements as a function of temperature were performed by placing a heating oven around the in situ X-ray cell. The oven had a Mylar™ window to allow the X-rays reach the in situ cell. Low temperature measurements were made by flowing nitrogen gas from a liquid nitrogen bath at a constant rate around the X-ray cell enclosed in the oven chamber. Temperature was monitored by a thermocouple in contact with the stainless-steel body of the in situ cell.

Electrochemical characterizations, other than those performed in the in situ cell, were performed either in Swagelok™ test cells or on plastic cells. The electrodes were in all cases fabricated utilizing Bellcore's newly developed PLiON™ technology [19]. The electrolyte used in all the

electrochemical cells was 1 M LiPF$_6$ in ethylene carbonate:dimethyl carbonate (2:1 v/v) solvent [20]. Swagelok™ cells were galvanostatically cycled through the use of a Mac Pile (Bio-Logic, Claix, France) MacIntosh controlled battery cycler. This cycler was used both in the galvanostatic and potentiodynamic modes. In the galvanostatic mode, the Li composition in the Li$_x$Mn$_2$O$_{4+\delta}$ material was calculated from the elapsed time and the current, assuming that the entire current was used in the intercalation/de-intercalation process. In the potentiostatic mode, the potential was scanned at a low rate of 39 mV/h. Plastic cells were cycled using a Smartcharger (Moli Energy, 1990, Vancouver, Canada) operating in a galvanostatic mode with at least 1% accuracy on the charge/discharge currents. Brunauer–Emmett–Teller (BET) specific surface area measurements were determined by means of a Gemini 2375 Sorption analyzer (Micromeritics, Norcross, GA, USA). Differential scanning calorimetry (DSC) was performed with a TA Instruments Model 910 DSC apparatus in air.

The average oxidation state for manganese was deduced by chemical analysis using the ferrous sulfate method [21]. Briefly, this method consists in dissolving the spinel with a quantity of ferrous ammonium sulfate in excess of a hot water/sulfuric acid solution. Once the dissolution is complete, the amount of Fe^{+2} is back-titrated with KMn$_2$O$_4$ solution (1 N). With such a method the average oxidation state of manganese can be determined with an accuracy of ±0.02. The results were confirmed by atomic absorption analysis of Li and Mn in these samples. The HF content was quantitatively characterized through back titration of the electrolyte solution in a 20:80 part ice water bath [22]. Titration was performed with a 0.1 N aqueous NaOH solution and a bromothymol blue indicator.

3. Results

3.1. The Li$_x$Mn$_2$O$_{4+\delta}$ series

The L$_x$Mn$_2$O$_{4+\delta}$ samples were fully characterized in terms of chemical, physical, structural, and electrochemical properties. The change of the cubic a-lattice parameter (as determined by X-ray diffraction) as a function of x is opposite to that of the average oxidation state of manganese (Fig. 1). As expected, the a-axis decreased while the average manganese valence increased, consistent with the larger amount of Mn^{4+}, whose ionic radius is smaller than that of Mn^{3+}. BET surface area measurements did not reveal meaningful changes as a function of x. All the samples had surface areas ranging from 0.6 to 0.8 m^2/g.

A Jahn–Teller distortion is known to occur in LiMn$_2$O$_4$ when the average valence is approximately 3.5 [23]. As reported by Yamada [24], lowering of the temperature can also induce a Jahn–Teller distortion. The decrease in temperature reduces the entropy contribution to the total energy of the system and subsequently increases the relative importance
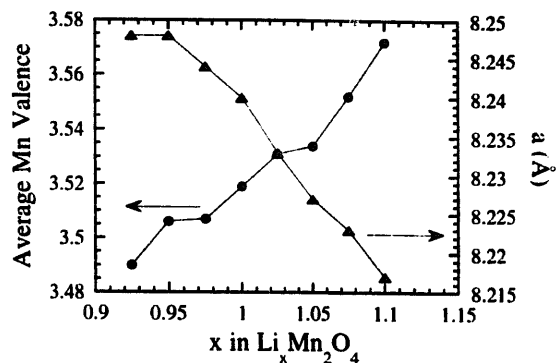

Fig. 1. Variation of the a-lattice parameter for the Li$_x$Mn$_2$O$_{4+\delta}$ series together with the average manganese oxidation state for each sample.

of the strain energy. In response to the change in energy contributions, the low-temperature version of the Jahn–Teller distortion is induced and is characterized by a relatively small c/a distortion of 1.01. Such a transition can be indirectly detected by DSC measurements through the presence of an exothermic peak in the DSC traces [24]. Among all the members of the series investigated down to −50 °C, only those with the lower x values (higher concentrations of the Mn^{3+} cation) have shown an exothermic peak, consistent with the Mn^{3+} induced Jahn–Teller distortion. With increasing x, the temperature at which this distortion occurs shifts to lower temperatures, and simultaneously the amplitude of the peak decreases, eventually vanishing for x greater than 1.00 (e.g. average manganese oxidation state of approximately 3.54) (Fig. 2), in agreement with Yamada's data [24]. The exothermic peak corresponding to the Jahn–Teller distortion was also observed to be generated for samples quenched from 800 °C instead of slowly cooling. This is expected based on the fact that the average oxidation state of manganese was found to be lower than 3.5 in the quenched spinel.

Interestingly, we found that the amplitude and onset temperature of the exothermic peak corresponding to the Jahn–
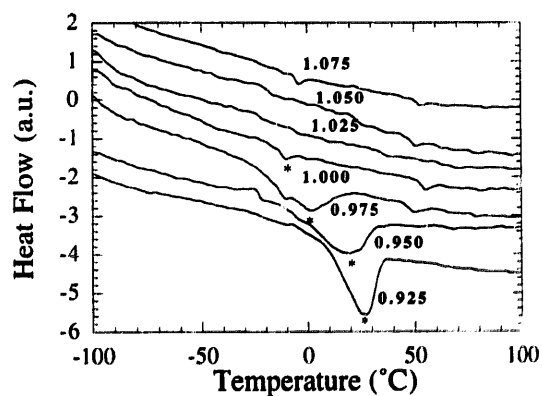

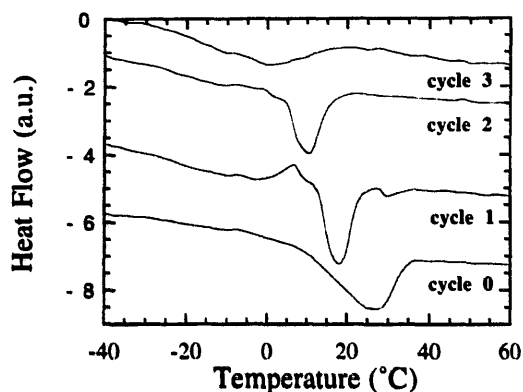Fig. 2. DSC measurements vs. temperature for members of the Li$_x$Mn$_2$O$_{4+\delta}$ series.

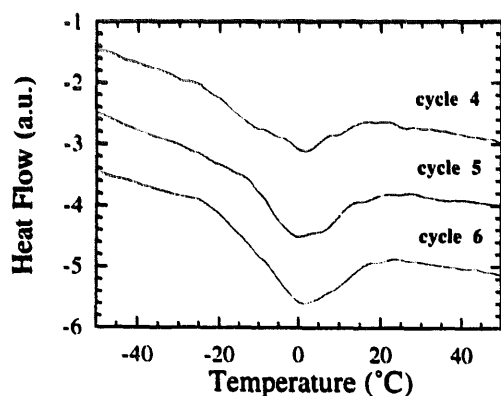Fig. 3. DSC spectra of a single $Li_{0.925}Mn_2O_4$ sample analyzed for scans 0-3.

Fig. 4. DSC spectra of a single $Li_{0.925}Mn_2O_4$ sample analyzed for scans 4-6.

Teller distortion has a tendency to rapidly decrease when the sample is thermally cycled repeatedly around the Jahn–Teller distortion's onset temperature. As Fig. 3 shows, repeated thermal cycling of the $Li_{0.925}Mn_2O_4$ sample results in a systematic decrease in the onset temperature and magnitude of the Jahn–Teller distortion as the sample was thermally cycled in the DSC apparatus. However, after four thermal cycles, the onset temperature eventually stabilizes at a lower temperature. Further thermal cycling resulted in a gradual increase in intensity and distinctness of the distortion (Fig. 4). We are presently investigating this hysteresis in more detail.

Galvanostatic charge/discharge curves were collected for all the samples. A theoretical discharge curve for an Li/ $LiMn_2O_4$ cell consists of a 4 and a 3 V intercalation plateau [4,25] of identical gravimetric capacity of 148 mAh/g, each corresponding to the insertion of one Li. The capacity for the first charge and discharge (expressed in ΔLi^+) is plotted as a function of x (Fig. 5) for the 4 V plateau. A noticeable difference between the charge and discharge capacities exists at low x. With increasing x, this difference decreases and eventually vanishes at $x = 1.025$. With respect to the capacity of the second plateau $LiMn_2O_4 \rightarrow Li_{1+x}Mn_2O_4$, it never reaches the theoretical value of $x = 1$ ($Li_2Mn_2O_4$), but was
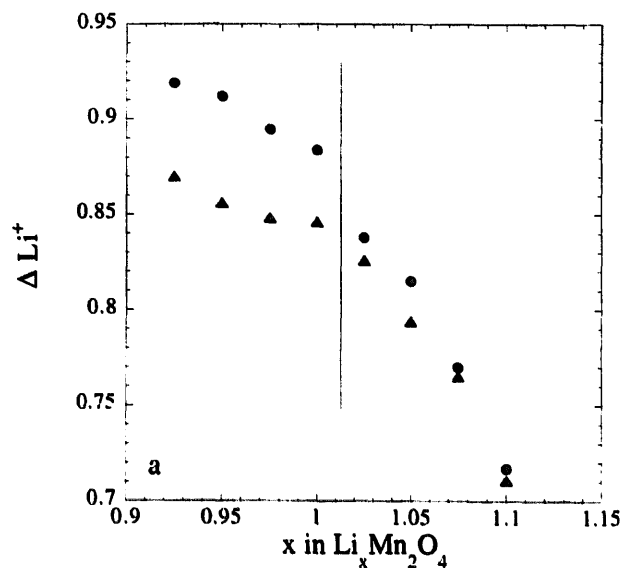

Fig. 5. Variation of (●) the first charge and (▲) first discharge capacity as a function of x for the $Li_xMn_2O_{4+\delta}$ series.

found to remain surprisingly low, ranging from 0.15 to 0.45 Li additional Li per 3d-metal. Largest 3 V capacities were obtained only for samples that were prepared from $LiNO_3$ instead of Li_2CO_3 as the Li precursor. A reversible $\Delta = 0.6$ on the 3 V plateau was obtained for the sample prepared by the nitrate method. The 3 V plateau originates from a two-phase insertion reaction consisting of the cubic phase and a Jahn–Teller distorted tetragonal phase and is known to be rate-limited due to diffusion considerations [26]. Therefore, the observed difference in capacity on the 3 V plateau can be attributed to the fact that the grain sizes are smaller in the nitrate-derived sample than those in the carbonate-made spinel. Finally, the influence of the Li nominal composition on
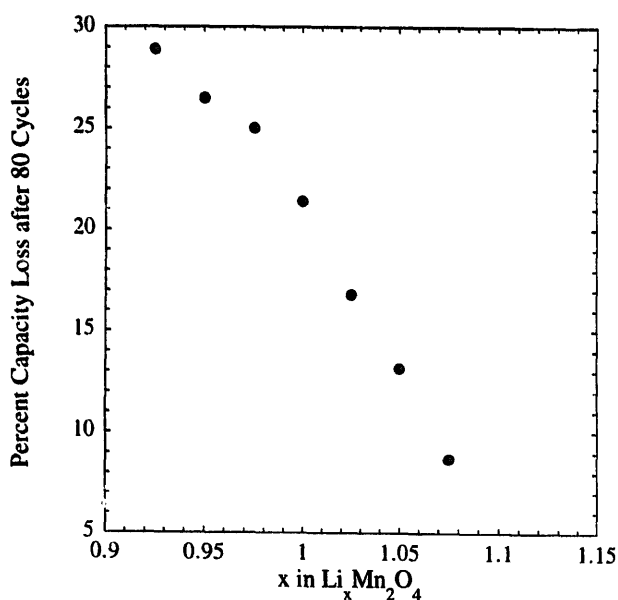

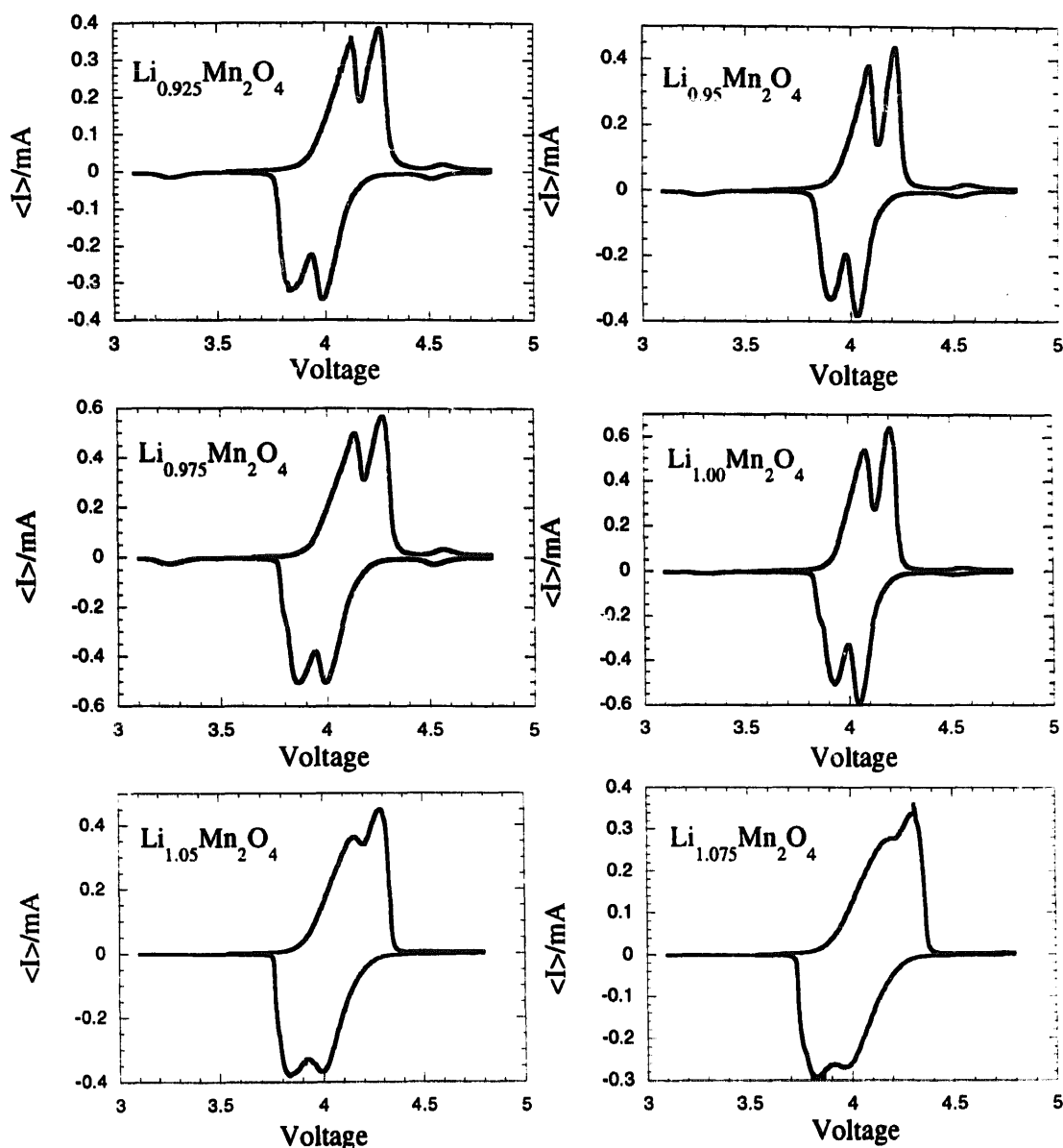Fig. 6. Percentage capacity loss as a function of x in $Li_xMn_2O_{4+\delta}$ after 80 cycles between 3.4 and 4.5 V.

Fig. 7. Cyclovoltammograms for the members of the $Li_xMn_2O_{4+\delta}$ series. The experiments were done between 3 and 4.8 V at a scanning rate of 25 mV per 0.64 h.

the capacity retention upon cycling was tested at room temperature. We found a systematic decrease in capacity loss after cycling $Li/Li_xMn_2O_{4+\delta}$ cells for 80 cycles between 3.4 and 4.5 V at $C/5$ (5 h per half cycle) as x was increased, the lowest capacity fading upon cycling (Fig. 6) was found for samples with the largest nominal x value.

Cyclic voltammetry was also performed in order to characterize subtle differences in the magnitude of the 4 and 4.1 V intercalation processes as a function of x in $Li_xMn_2O_{4+\delta}$. Among the most noticeable differences (Fig. 7) is the decrease in the resolution of the 4 and 4.1 V peaks for samples with $x > 1.00$. As will be confirmed shortly by in situ XRD measurements, such a change suggests a different intercalation process between these various samples. Besides these two major peaks are the occasional 4.5 and 3.3 V Li-insertion

peaks that have been previously reported [27,28,11]. The variation of the intensity of these two reactions as a function of x in the initial spinel $Li_xMn_2O_{4+\delta}$ is graphically portrayed in Fig. 8(a) and (b). The intimate relationship of these peaks are shown in these figures, as the intensity variations between the 3.3 and 4.5 V reactions clearly mirror each other. Such a direct relation was previously reported by Gao and Dahn [28] and, based on this relation, concluded that these two peaks have the same origin in the oxygen stoichiometry of the spinel.

3.2. The $Li_{1.05}Mn_{1.95}O_4$ HT series

The HT series, which consisted of a series of $Li_{1.05}Mn_{1.95}O_4$ samples re-annealed at various temperatures,

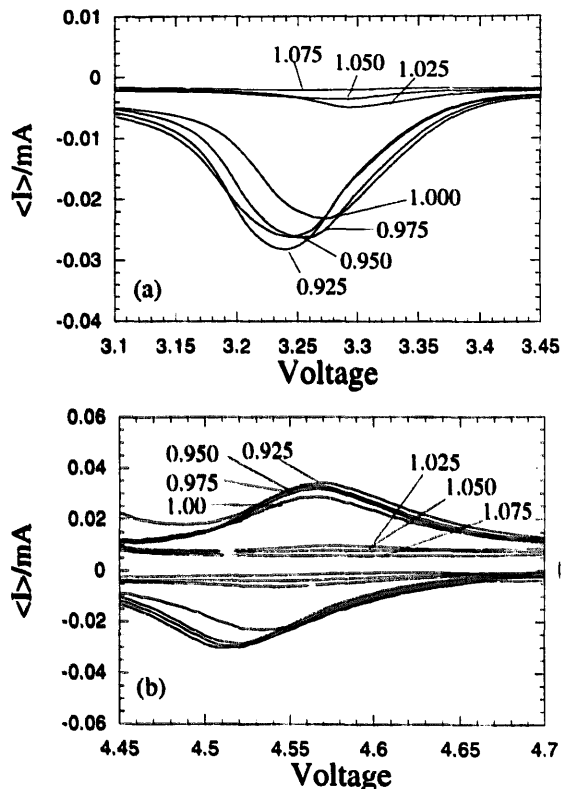Fig. 8. Cyclovoltammograms of the various members of the $Li_xMn_2O_{4+\delta}$ series showing the evolution of the (a) 3.3 and (b) 4.5 V) peak as a function of x. The experiments were done between 3 and 4.8 V at a scanning rate of 25 mV per 0.64 h.
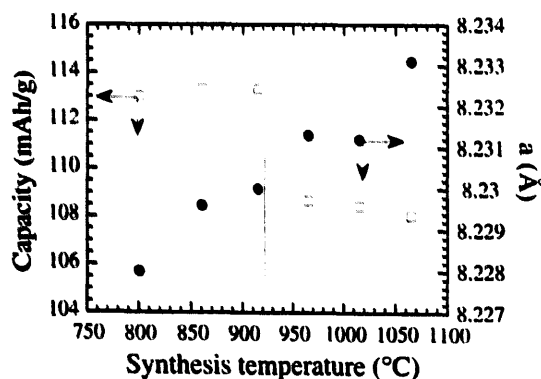

Fig. 9. Variation of (□) the capacity for the members of the HT series together with the variation of (·) the a-lattice parameter. The line indicates the temperature at which the cubic-tetragonal phase transition is occurring.

was also systematically studied. Fig. 9 shows the variation of the lattice parameter together with the variation of the reversible capacity. As reported previously, annealing at elevated temperatures resulted in the loss of oxygen, reduction of the spinel, and formation of a tetragonal phase at 915 °C [11]. The temperature at which the cubic to tetragonal phase transition occurs in the spinel is indicated by a vertical line. At the same slow cooling rate, note the importance of the synthesis temperature, with the samples having the largest capacity being those prepared at temperatures below 915 °C. It was

also found that samples synthesized at the highest temperature exhibit the largest irreversible capacity between the first charge and first discharge.

The capacity fading at 25 °C for cells based on the HT series samples is shown in Fig. 10. Two different fading rates can be observed depending on the sample's synthesis temperature similar to the reversible capacity trend described above. Those spinels annealed at temperatures below the cubic-tetragonal phase-transition temperature show a very low fading over the first 50 cycles while those prepared at temperatures higher than the cubic to tetragonal phase transition show a high fading rate, at least during the first 50 cycles, which is similar to the behavior shown by the quenched $Li_{1.05}Mn_{1.95}O_4$ samples or those deficient in Li (e.g. $Li_{0.925}Mn_2O_4$). The variation of the average oxidation state as a function of the annealing temperature is shown in Fig. 11. The average oxidation state remains constant for samples prepared below the cubic-tetragonal transition temperature and decreases slightly for those prepared at temperatures above 1000 °C. Within the series, a decrease in surface area (e.g. a coarsening of the powders) from 0.8 to 0.14 m^2/g (Fig. 12) was observed, as expected, with increasing annealing temperatures. Changes in sample surface areas could affect Li diffusion, and thereby be at the origin of the observed difference in cycling efficiency. However, constant fading
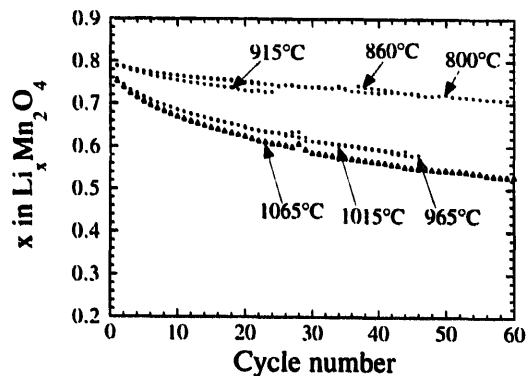

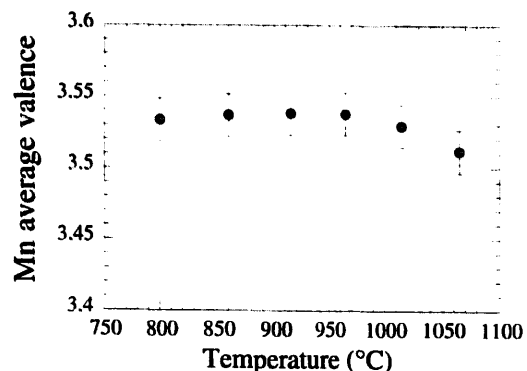Fig. 10. 25 °C cycling of $Li_{1.05}Mn_{1.95}O_4$ HT samples annealed at various temperatures. Cycling was performed between 3.4 and 4.5 V at C/5.

Fig. 11. Average oxidation state of manganese vs. annealing temperatures of $Li_{1.05}Mn_{1.95}O_4$ samples.
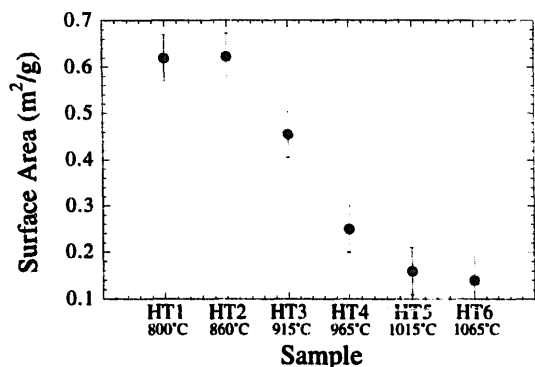
Fig. 12. Variation of BET surface areas as function of annealing temperature for HT $Li_{1.05}Mn_2O_4$ samples.

rate at either $C/2$ or $C/50$ charge/discharge rate rules out the Li-diffusion argument.

To explain such a change in behaviour, is interesting to note that the decrease in capacity and cycle life with an increase in irreversible capacity loss corresponds with an increase in the a-axis lattice parameter that reaches values greater than 8.23 Å (Fig. 9) for samples annealed at the higher temperatures. This value was previously set as a necessary condition in the process of screening electrochemically optimized $Li_xMn_2O_{4+\delta}$ powders [11–13]. Post reaction analysis by XRD reveals that the $Li_{1.05}Mn_{1.95}O_4$ samples annealed above 915 °C shows presence of a secondary phase consisting of Li_2MnO_3, consistent with recent reports of Gao and Dahn [29] and Thackery et al. [30]. The fact that an Li-rich spinel phase was used as the initial material for the reaction can easily account for the presence of a phase separation at high temperatures   ($Li_{1.05}Mn_2O_4 \rightarrow Li_{1.05-2y}Mn_{2-y}O_4 + y(Li_2MnO_3)$). However, the detrimental factor to the cycle life in this reaction is not the electrochemically inert Li_2MnO_3, but is in effect the electrochemically active cubic-spinel phase. With the loss of Li to the Li_2MnO_3 phase, the cubic phase has now a stoichiometry of Li of $x < 1.05$. This evidence is supported by the a-lattice parameter change to values > 8.23 Å dictating a change in average oxidation state in the bulk of the cubic spinel. Such a change was not detected easily by the average oxidation-state measurement (Fig. 11) as the reduced manganese valence state in the cubic spinel was offset by the formation of Mn^{4+}-rich Li_2MnO_3 secondary phase. As we have shown before for the traditionally prepared materials, samples with nominal x values < 1.025 cycle poorly and have larger irreversible capacity losses (Fig. 5). In addition, the loss of Li and manganese to the Li_2MnO_3 impurity phase can explain the loss of reversible capacity during the first cycle (Fig. 9), as there is simply less-active material. For both the HT samples and the $Li_xMn_2O_{4+\delta}$ series, the performance at 55 °C cycling was found to follow the same trend as we have previously shown for the room-temperature cycling, with the largest fade being observed for the samples having the largest a-lattice parameter, while most of the samples retained a 0.8 m^2/g specific surface area.

This decomposition of the lithiated spinel phase to a two-phase system consisting of Li_2MnO_3 and a cubic spinel of lower Li nominal composition x in $Li_xMn_2O_4$ was also found for $Li_{1.05}Mn_{1.95}O_4$ samples quenched from 815 °C. In effect, stoichiometries of the electrochemically active spinel in the HT samples (>915 °C), the quenched sample, and $Li_xMn_2O_4$ samples with $x < 1.025$ are approximately the same in terms of the average manganese oxidation state, thus explaining the similar large a-lattice parameter (which is inversely proportional to the average oxidation state of the manganese cation) and poor cycling performance.

3.3. Effect of Li precursor

The capacity fading of two different $LiMn_2O_4$ samples (samples made from different Li precursors: $LiNO_3$ and Li_2CO_3, but treated identically) is compared at room temperature and at 55 °C (Fig. 13) in Li-ion cells. In these samples as opposed to the samples discussed above, the 25 and 55 °C cycling trends did not follow the same trends. (Note that the cycling behavior at 25 °C is identical for both samples while it markedly different at 55 °C, with the nitrate-based sample cycling poorly). The main difference between the nitrate and carbonate samples are the changes in the specific surface areas (0.8 m^2/g for the Li_2CO_3 and 3.6 m^2/g for the $LiNO_3$). As both samples cycled well at room temperature, it should be stressed that room-temperature cycling performance can only be used as a necessary but not sufficient condition to screen electrochemically optimized $LiMn_2O_4$ materials.

3.4. Self-discharge

Elevated temperature capacity loss in the delithiated state was characterized as follows: C/electrolyte/$LiMn_2O_4$ Li-ion cells were cycled five times at room temperature between 2.5 and 4.5 V at a rate of $C/5$ concluding with a final charge to 4.5 V. The cells were then placed at open circuit for 1 week in an oven at 55 °C ± 1 °C. Afterwards, the cell was discharged and recharged five times at the same current rate ($C/5$) prior to being left another week at open circuit at 55 °C and so on.
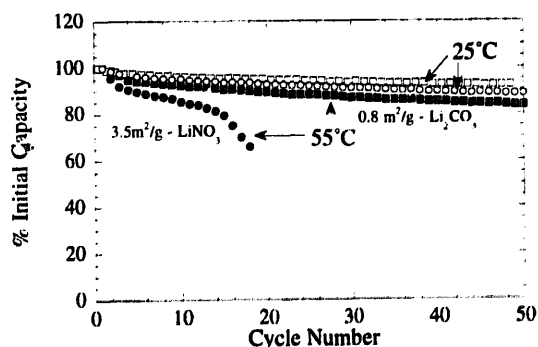

Fig. 13. Room temperature and 55 °C cycling of $Li_{1.05}Mn_2O_4$ spinels fabricated with lithium precursors of (O,●) $LiNO_3$ and (□,■) Li_2CO_3. Cycling was performed between 3.4 and 4.5 V at $C/5$.
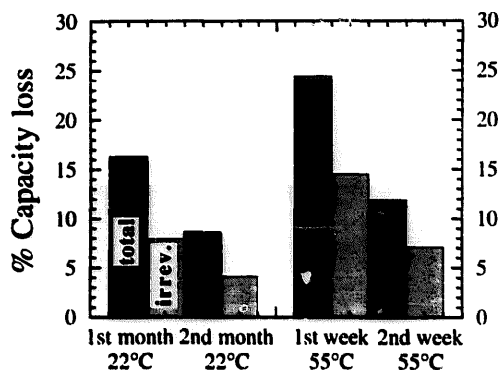
Fig. 14. Self-discharge for plastic $C/Li_{1.05}Mn_{1.95}O_4$ Li-ion cells measured at 22 and 55 °C. For the numbers to be significant measurements over the course of 2 months were performed at room temperature instead of one week at 55 °C.

Fig. 15. Structural stability of the λ-MnO_2 phase as determined by the high temperature Guinier-Lenne Camera. Note that the phase transformation occurs around 210 °C.

From the first discharge and charge after storage we deduced the reversible and irreversible capacity loss. Independently of the samples, a drastic increase in the irreversible capacity loss on storage at 55 °C was observed when compared with room temperature (Fig. 14). Such trends are typical, with a large initial loss followed by losses decreasing in magnitude over the subsequent weeks. In an attempt to explain the observed trends in high-temperature performance and their origin, we investigated the stability of delithiated samples, the mechanism of Li insertion and the morphology of the electrodes.

3.5. Stability of the delithiated λ-Mn_2O_4 phase

Delithiation of $Li_xMn_2O_4$ results in the formation of the metastable λ-Mn_2O_4 phase that decomposes to β-MnO_2 at temperatures ranging from 100 to 250 °C, and in some cases, ϵ-Mn_2O_4 may be detected as an intermediate in the progression of the decomposition [8]. The rutile structure of the β-phase is electrochemically inactive at 4 V and exhibits limited Li insertion at lower voltages before the transformation to a tetragonal variation of $LiMnO_2$ [31,32]. When C/electrolyte/$LiMn_2O_4$ Li-ion cells are in the charged stage, the composition of the positive electrode is λ-Mn_2O_4. Therefore, we decided to investigate whether the 55 °C storage properties of $LiMn_2O_4$-based Li-ion cells could be correlated with the decomposition temperature of the λ-Mn_2O_4 phase. Several Swagelok™ cells were prepared using various $LiMn_2O_4$ samples and the cells were charged to 5 V versus Li/Li$^+$. Charging to such high voltages assured the removal of all electrochemically removable Li ions, although full removal of all Li ions is not possible in some cases. For example, full Li de-intercalation from the spinel of $Li_{1.05}Mn_{1.95}O_4$ compositions is not possible due to a redox limitations as these 'oxidized' compositions are Mn^{3+} starved. Also, a small quantity Li is located in the inacccessible $16d$ octahedral sites. These de-intercalation limitations are shown in the in situ XRD studies discussed in the next section. In spite of this,
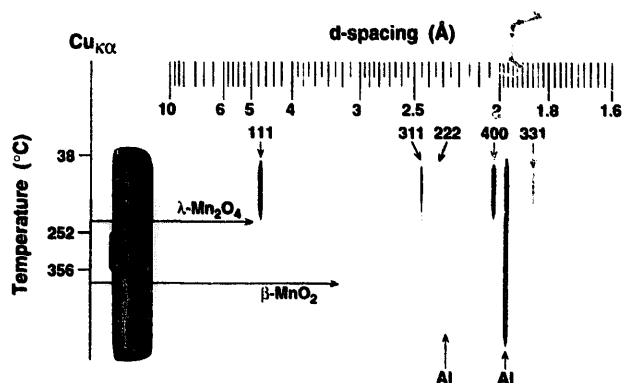
we will consider all these samples as approximating the λ-MnO_2 structure. After charging, the resulting cathode material was recovered, washed in acetone to dissolve the binder and the powders were recovered. The loose powders were then mounted in a high-temperature Guinier-Lenne camera, and the temperature of the sample was raised at a rate of 0.2 °C/min. With increasing temperature we noted the disappearance of the main Bragg peaks corresponding to the cubic phase at temperatures of about 200 °C (Fig. 15). Independently of the sample-cooling conditions (quenched versus slowly cooled) or their nominal compositions (low versus high x) the λ- to β-phase transformation for all samples occurred at 200 ± 15 °C. However, these samples show large differences in their 55 °C behavior, clearly indicating that the thermal stability of the λ-Mn_2O_4 phase cannot be the basis used to explain the poor elevated temperature performance.

3.6. Single-phase versus two-phase de-intercalation process

The question whether or not the Li de-intercalation/intercalation process in the spinel ($LiMn_2O_4 \rightarrow \lambda$-$Mn_2O_4$) is a single-phase or a two-phase process has been the subject of numerous contradictory reports [33,34]. It was recently reported by Xia and Yoshio [34] that depending on the sample history, both processes can exist. Thus, could such a difference in the Li-intercalation process be at the origin of the poor electrochemical performance of some samples at 55 °C?

To shed some light on this issue, we studied the Li de-intercalation mechanism in various $LiMn_2O_4$ samples by in situ XRD using a newly developed in situ X-ray electrochemical cell [18] that can properly operate up to 5 V oxidizing voltages. The in situ X-ray data are reported for several samples, starting with the HT series (Fig. 16). Note that in this case, XRD of HT1 (annealed at 800 °C) revealed that only a single-phase intercalation process was observed with, however, a small slope change in the lattice parameter versus a-composition curve at approximately $x = 0.5$, which becomes
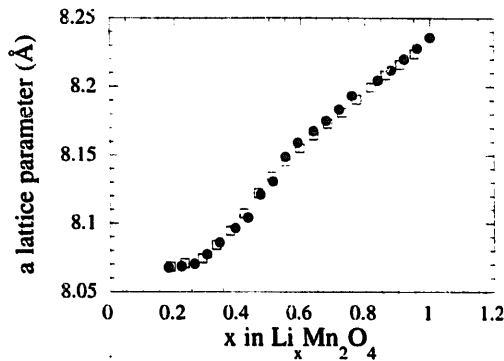
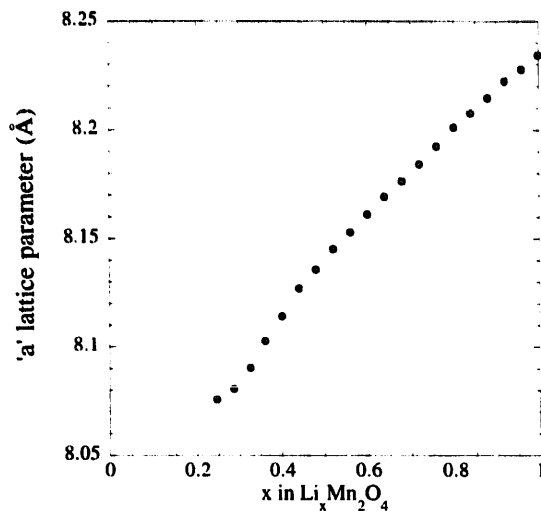Fig. 16. Variation of the a-axis lattice parameter as a function of the Li de-intercalation for (□) HT1 and (■) HT4.

Fig. 17. Variation of the a-axis lattice parameter as a function of the Li de-intercalation for the HT1 sample after being ball-milled.

Fig. 18. Variation of the a-axis lattice parameter as a function of the Li de-intercalation for the (a) $Li_{1.05}Mn_{1.95}O_4$ sample and (b) $Li_{0.95}Mn_2O_4$ sample.

slightly more noticeable for HT4 (annealed at 916 °C). Since for samples, such as HT1, we had measured a large particle size (small surface area), we decided to mill the HT1 sample and to repeat the experiment to eliminate a possibility that the single-phase Li-extraction process was due to non equilibrium conditions brought about by diffusion gradients being developed within the large particulates. Independent of the surface area, while the lattice parameter remained constant, we observed only a single phase (Fig. 17). This was the first indication that the single-phase versus double-phase de-intercalation/intercalation process cannot completely distinguish between good and poor materials as both HT1 and HT4 retain a single-phase Li-extraction process at 25 and 55 °C, but the former has good cycling performance while the latter cycles poorly.

Similar type of in situ measurements were performed for the $Li_xMn_2O_{4+\delta}$ series. We found that the spinel $Li_xMn_2O_{4+\delta}$ with low x shows a two-phase Li-intercalation process that becomes a single phase at high x ($x \geq 1.025$). As Fig. 18 shows, a sample with a nominal composition of $x = 1.05$ (Fig. 18(a)) retains a single-phase Li-extraction process, while samples with $x = 0.95$ (Fig. 18(b)) exhibit a two-
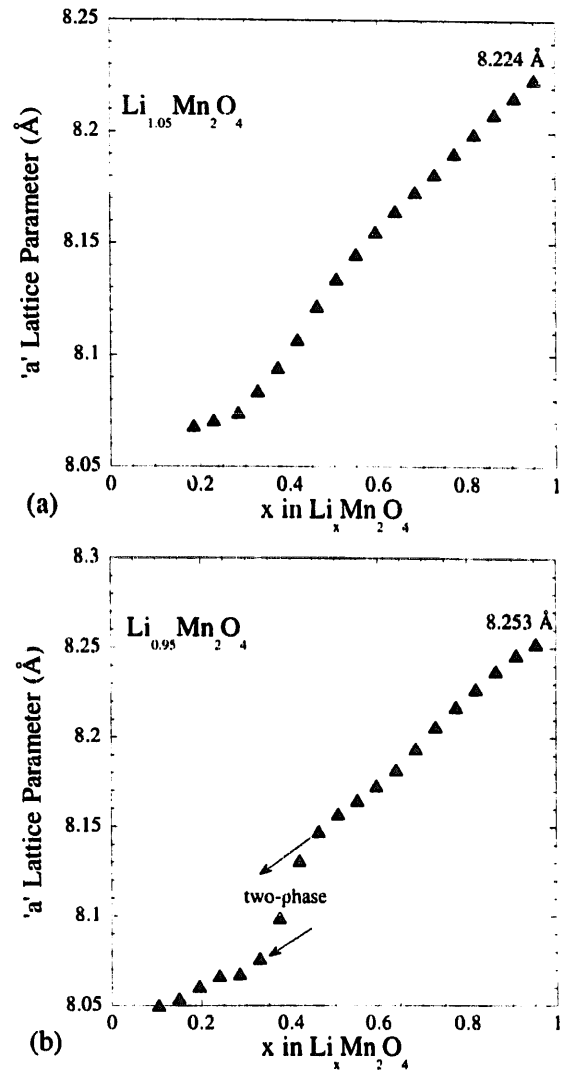
phase extraction process. This is indeed the structural analog to the single- or two-phase Li-insertion/extraction reaction characterized by the cyclic voltammetry scans shown in Fig. 7. A difference between the low x and high x samples is the average manganese oxidation state, which has been previously shown to be inversely proportional to the a-lattice parameter (Fig. 1). To determine whether the a-axis value of $LiMn_2O_4$ could be indicative of the nature of the de-intercalation/intercalation process, we investigated $Li_{1.05}Mn_{1.95}O_4$ samples quenched at 800 °C that have large a-axis values, similar to those for samples of low x nominal composition, and invariably found a two-phase intercalation process (Fig. 19). Other than quenching the sample, another way to obtain lattice parameters greater than 8.23 Å, as will be reported elsewhere [35], is to perform anionic substitution (e.g. replacing O by F). In situ X-ray data on such partially substituted $LiMn_2O_{4-y}F_y$ samples indicate that these samples also exhibit a two-phase intercalation process and retain poor cycling characteristics.
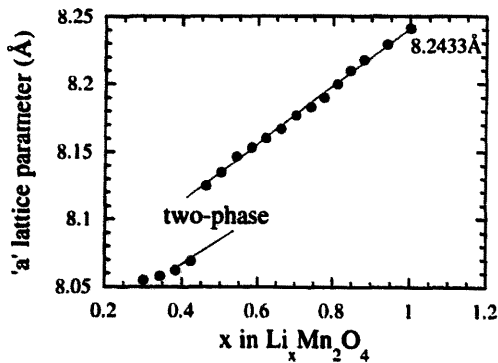
Fig. 19. Variation of the a-axis lattice parameter as a function of the Li de-intercalation for a quenched sample of nominal composition $Li_{1.05}Mn_{1.95}O_4$.

In general, all phases which shared poor cycling efficiencies retained the two-phase Li-extraction process. Since the storage properties of $LiMn_2O_4$-based Li-ion cells worsen at elevated operating temperatures, we studied how the two-phase Li-de-intercalation/intercalation process evolved with temperature. Do normally single-phase reactions that cycle well at room temperature transform to biphasic reactions at elevated temperatures to account for the poor performance?

In situ XRD patterns of $Li_{1.05}Mn_{1.95}O_4$ samples which are normally single phase at room temperature, were found to remain single phase at 55 °C. More interesting, however, were results obtained for samples which have two-phase Li-insertion extraction reactions at room temperature. In situ XRD measurements as a function of the temperature were performed on a quenched sample showing at room temperature a distinct two-phase intercalation process. For such a measurement, the in situ X-ray cell was discharged to the value of $x = 0.5$ for which the splitting of the hkl Bragg peaks was evident. The cell was then placed at open circuit, and the sample temperature was changed. After each sequence of measurement, the cell temperature was returned to room temperature to ensure that the original XRD pattern could be recovered and to check whether the reaction was truly reversible. We noted that increasing the temperature resulted in the two cubic phases converting into one as shown by the coalescence of the Bragg reflections in Fig. 20 (for clarity reasons we only reported the range of the diffraction patterns where the splitting can be clearly visualized). The splitting within the two Bragg peaks corresponding to the (333) and (440) reflections, which is the largest at 0 °C, decreased with increasing the temperature to become a single peak when the temperature reached 50 °C. The reflections continued to narrow up to 70 °C. This reversible process is indicative of a miscibility gap [36].

With respect to high- and room-temperature performance, such a finding suggests that the observed 55 °C self-discharge or poor cycling within the spinel cannot be explained in terms of the monophasic versus biphasic Li-de-intercalation/intercalation process, since at 55 °C the intercalation process is monophasic for all samples while they show drastic differences in their storage and cycling performance at room and
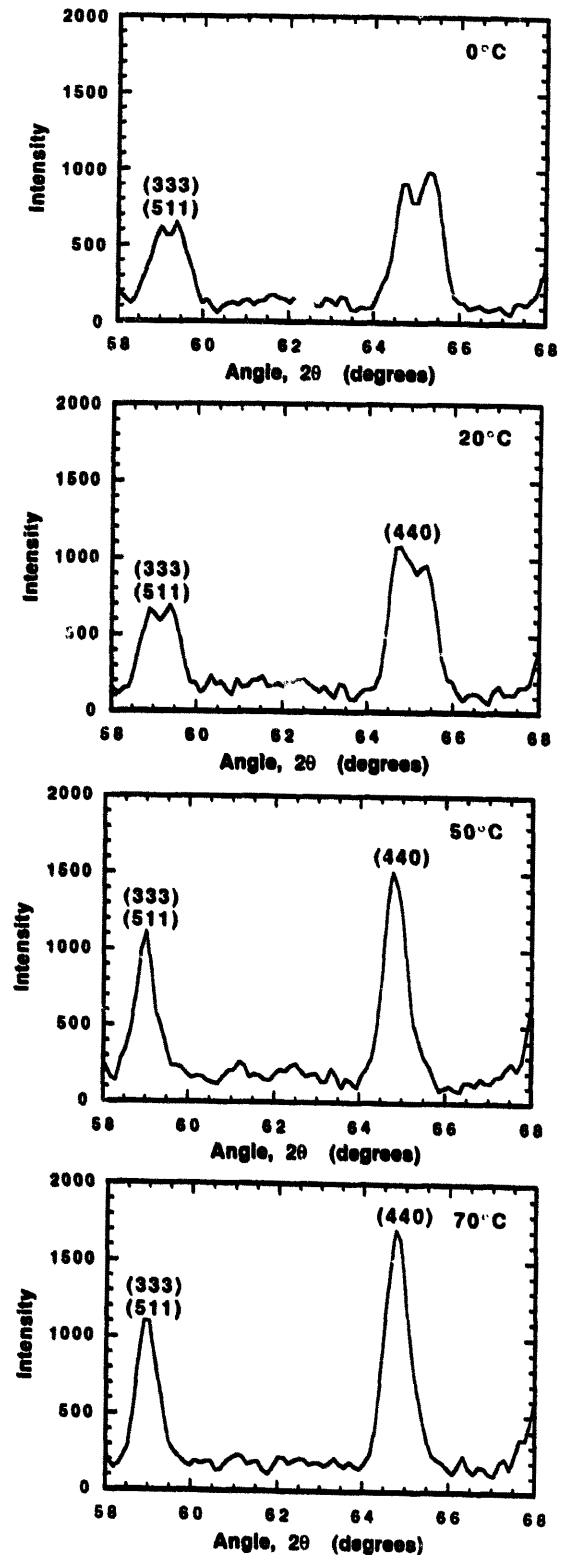
Fig. 20. Variation of the XRD gram as a function of the temperature for a quenched sample of nominal composition $Li_{1.05}Mn_2O_4$.

elevated temperatures. However, from our in situ X-ray survey of a wide variety of samples, one can state that the best $LiMn_2O_4$ samples exhibiting enhanced 55 °C storage performance are those for which the room temperature Li-intercalation/de-intercalation process is monophasic, in

agreement with recently published data [34]. The question remains, however, whether this physiochemical feature is directly responsible for the enhanced performance, or rather an artifact of the true stabilization mechanism. A closer look at the intercalation process should shed light on this question.

As Fig. 7 portrays, the Li-insertion/extraction process in the $Li_xMn_2O_{4+\delta}$ samples with $x < 1.025$ can also be qualitatively described as two peaks separated by a trough, being consistent with an Li-ion ordering reaction. This relationship was first realized by Gao et al. [37]. In their paper, a mechanism was proposed to explain for the disappearance of the ordering reaction for x values greater than 1.00. At $x > 1.00$ it is known that the excess Li occupies $16d$ octahedral sites in the manganese sublattice. In this case, it was theorized and supported by modeling that Li^+ occupation of the octahedral site would result in the intercalated Li ion on the $8a$ tetrahedral site to be pinned by the larger electron density available on the oxygen anion. These 'pinned' Li ions would then make it difficult for Li ions to order in the $8a$ sublattice. This is consistent with the Li-intercalation mechanism first proposed by Tarascon et al. [11] in 1994, in which the short range interaction energy between nearest neighbor Li-Li interactions on tetrahedral sites was determined to be 0.05 eV. In order to maintain a low energy status, the intercalation was proposed to occur in an ordered fashion. In this process alternate tetrahedral sites were filled to $x = 0.5$. At $x > 0.5$ nearest neighbor Li ions are filled at a higher energy level 0.2 eV (four coordination, 0.05 eV per interaction) due to the interaction energy. The important point is that the interaction energy controls the degree of the two phase reaction.

As we have shown in Fig. 20, an increase in temperature results in the coalescence of the Bragg peaks associated with the two cubic-phase reactions and results in a single-phase extraction. This is consistent with and a proof that the reaction is indeed an ordering reaction. As temperature is increased, the free energy of the system is governed more and more by the entropy contribution. Thus, as temperature is increased, the disorder brought about by the thermal energy dissolves the energetic benefit of ordering and results in a single-phase extraction. It is unlikely that the ordering reaction has any macroscopic effect on the cycling efficiency of the spinel, as the strains developed as a result of the reaction are minimal due to the minimal volume change and most importantly are isotropic due to the cubic lattice structure which minimizes the resulting strain at the incoherent grain boundaries.

3.7. Effect of surface area

There are many conflicting reports concerning the importance of large versus small specific surface area of the spinel $LiMn_2O_4$ with respect to its electrochemical performance as large surface area has been a traditional goal of MnO_2 for primary batteries. Small particulate size has been targeted in many recent reports concerning the processing of $LiMn_2O_4$ in order to optimize the power rates of the spinel. To shed some light on this issue, we took an $Li_{1.05}Mn_{1.95}O_4$ slowly-
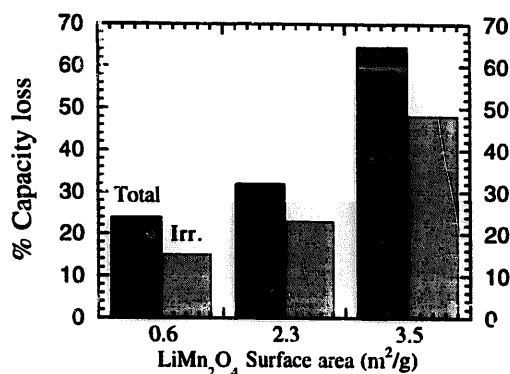

Fig. 21. Effect of the surface area of $Li_{1.05}Mn_{1.95}O_4$ powders obtained by ball-milling on their 55 °C storage performance.

cooled sample with a surface area of $0.65 \text{ m}^2/\text{g}$ and milled this sample to obtain powders with specific surface areas of 2.28 and $3.66 \text{ m}^2/\text{g}$, respectively. Milling was performed carefully in order not to induce a substantial number of structural defects, as determined by X-ray diffraction. The storage results for the 'as made' samples and the milled samples are summarized in Fig. 21. As can be seen, the self-discharge increases with the surface area. The effect of the surface area on the 55 °C storage performance is drastic, and consistent with our previous explanation that the electrolyte decomposition at high voltages catalyzed by the electrode surface is responsible for self-discharge during storage. This is also consistent with the sharp contrast between the 25 and 55 °C cycling efficiencies of the high surface-area spinel obtained from the $LiNO_3$ precursor (Fig. 13) which has a large surface area. The importance of the positive electrode surface area on the storage performance of the resulting Li-ion cell is not specific to $LiMn_2O_4$ but common to any oxide materials operating at oxidation voltages greater than 4 V versus Li. It is important to recall that while large surface areas electrodes are much desired for primary cells (irreversible chemical reaction), they are detrimental to the proper functioning of rechargeable Li-ion cells where the electrolyte is always operating at high oxidizing voltages.

3.8. Manganese dissolution

The evidence for manganese dissolution in $LiMn_2O_4$-based Li-ion cells has long been reported and sometimes proposed as the possible cause of the poor storage performance of Li-ion cells (e.g. large self-discharge) at elevated temperatures. So is there a correlation between electrolyte decomposition and manganese dissolution or first, does the manganese dissolution correlate with the $LiMn_2O_4$ specific surface area? The manganese dissolution at 55 °C was measured for $LiMn_2O_4$ samples of the same nominal composition but made from either Li carbonate, hydroxide, or nitrate resulting in $LiMn_2O_4$ specific surface areas of 0.8, 0.7 and $3 \text{ m}^2/\text{g}$, respectively. For such measurements, plastic electrodes were made using Bellcore's PLiON™ technology. The plastic electrodes

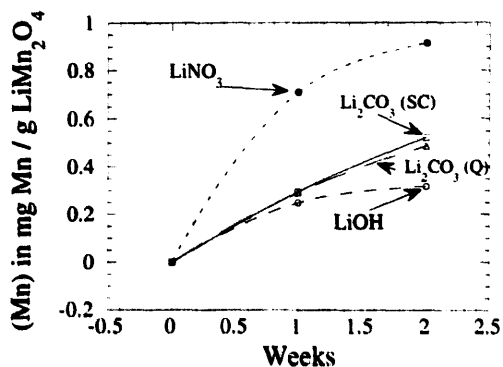Fig. 22. Comparison of the manganese dissolution as a function of time for non cycled fresh Li$_{1.05}$Mn$_{1.95}$O$_4$ electrodes made using either LiOH, Li$_2$CO$_3$, LiNO$_3$ precursors and for a non cycled fresh electrode of nominal composition Li$_{1.05}$Mn$_2$O$_4$ made from the carbonates that was quenched. The electrodes were placed into 25 cm^3 of electrolytes maintained at 55 °C.

Fig. 23. Effect of surface chemical treatments of LiMn$_2$O$_4$ powders on their 55 °C storage performance.

containing 500 mg of active material and 50 mg of carbon black were, after extraction of DBP by ether, pumped in vacuum overnight at 60 °C and placed into a dry-box. The resulting electrode was inserted into a polypropylene vessel containing 25 cm^3 of fresh electrolyte (1 M LiPF$_6$ in 2/3 ethylene carbonate and 1/3 dimethyl carbonate) and placed on a heating plate at 60 °C. Electrolyte samples were taken once the electrode was first inserted into the electrolyte (time $t = 0$) and there after every week over the course of a two-week period, and analyzed for their manganese and HF contents.

The evolution of the manganese content as a function of time is shown in Fig. 22 for standard Li$_{1.05}$Mn$_{1.95}$O$_4$ slow cooled, quenched, and those made with an Li-nitrate and LiOH precursor. A similar trend was observed for the evolution of the HF content with time. Note that the Li$_2$CO$_3$, LiOH-based, and quenched Li$_{1.05}$Mn$_{1.95}$O$_4$ samples have the lowest manganese dissolution while the nitrate-based samples with a large surface area exhibit the largest manganese dissolution. Thus, both the manganese dissolution and electrolyte breakdown are proportional to the LiMn$_2$O$_4$ specific surface area, but this does not necessarily imply that they are related. Two chemical reactions governed by thermodynamic mechanisms could easily scale with the specific surface area while being totally independent. Manganese dissolution must proceed through the following dismutation reaction $2\text{Mn}^{3+} \rightarrow \text{Mn}^{4+} + \text{Mn}^{2+}$ (with Mn^{2+} going into the solution) that occurs in presence of acid traces [4]. The LiPF$_6$-based electrolyte is known to always contain small amounts of HF (see sample specifications). Our experience indicates that HF amounts (as determined by acid–base titration) in the electrolyte can easily increase as a result of electrolyte breakdown generated by elevated temperatures or any small quantities of water, thus resulting in an increase in the manganese dissolution. Control of HF content is critical to the successful implementation of LiMn$_2$O$_4$-based Li-ion technolgy to the commercial arena.
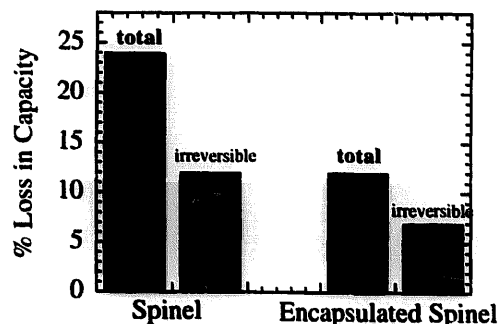
It is conceivable that the larger the surface area of LiMn$_2$O$_4$, the larger the amount of surface manganese atoms exposed to electrolyte will be, and thereby the larger the dissolution. Therefore, it is critical that the issue of manganese dissolution is addressed for the successful implementation of LiMn$_2$O$_4$ into Li-ion batteries. So a solution to this problem could be, as it has already been suggested, to trap HF as soon as it has been formed by means of HF scavengers [38]. Another solution can be proposed if one realizes that manganese dissolution occurs at spots where the electrolyte and the manganese surface atoms are in contact (e.g. at the LiMn$_2$O$_4$/electrolyte interface). Therefore a possible solution to this interfacial problem is to minimize this contact area by creating a shell of inorganic material around each LiMn$_2$O$_4$ particle that will prevent the electrolyte contact while allowing the Li ions to go through. This will have a two-fold benefit in that it will reduce HF induced disproportionation/dissoluion reactions, and also minimize electrolyte decomposition on the surface of the spinel by the formation of this inorganic passivation layer. Such a simplistic view has been successfully tried by means of surface chemistry as will be reported elsewhere [39] and has resulted in materials with enhanced 55 °C storage performances (Fig. 23).

4. Discussion

From the data presented here for the Li$_x$Mn$_2$O$_{4+\delta}$ series, HT series, quenched, preliminary data on fluorine-doped samples and of previous data on tetragonal samples one can isolate the physical and chemical characteristics that an LiMn$_2$O$_4$ specimen should have to ensure the assembly of C/LiMn$_2$O$_4$ Li-ion cells with enhanced capacity retention and low self-discharge in the delithiated state at 55 °C. Such Li$_x$Mn$_2$O$_{4+\delta}$ specimens must have an x value of at least 1.05, an average oxidation state for manganese greater than 3.55, a-lattice parameter lower than 8.23 Å, intercalate/de-intercalate Li ions at room temperature through a single-phase process and finally have a surface area that does not exceed 1 m^2/g.

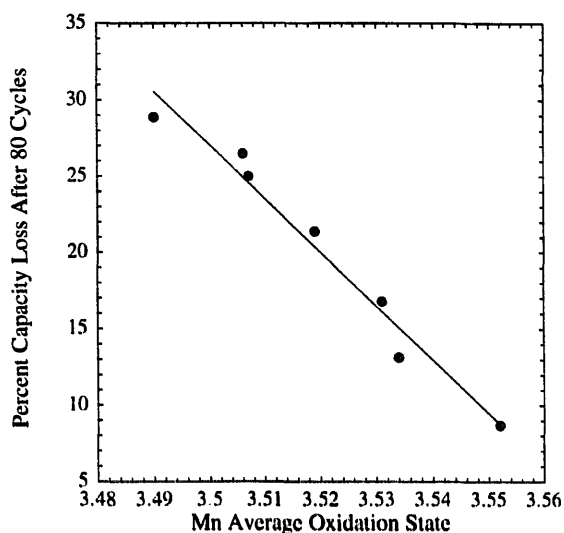As an attempt to rationalize why both room temperature and 55 °C capacity loss upon cycling are greater for some

Fig. 24. Percentage capacity loss after 80 cycles vs. initial average valence state of manganese in $Li_xMn_2O_{4+\delta}$.

samples, we performed a cross comparison of all the samples investigated. Three major characteristics, namely (i) the presence of the 3.3 and 4.5 V plateaus; (ii) the existence of biphasic versus single-phase Li extraction, and (iii) the average oxidation state or manganese occupation can be used to distinguish these samples. The samples with x greater than 1 show excellent retention upon cycling. In contrast, it is interesting to note that all the samples with x lower than 1, tetragonal (quenched 915 °C), quenched (800 °C) or F-substituted samples have a similar characteristic, namely a large capacity loss over the initial 50 or so cycles. The only thing that these last samples have in common is the biphasic extraction at room temperature and low average manganese state. The tetragonal phase does not have any 3.3 or 4.5 V plateaus, therefore, the difference in capacity fading observed must be due to either changes around the average oxidation state or the biphasic region.

The observation that the Li-extraction process is monophasic at 55 °C for all the samples while their storage performance and cycling at elevated temperature is still poor, leaves us with only the average oxidation state as a possible argument to account for the capacity loss with the reduced samples. This is consistent with the observation that the capacity loss after 80 cycles scales perfectly with the average manganese oxidation as is clearly seen in Fig. 24. This is further evidence against that the 3.3 or 4.5 V reactions are not the origin of the poor cycling efficiencies. This is apparent if you look at the progression of these reactions (Fig. 8(a) and (b), respectively) as none of these features scale linearly with the room temperature capacity fade. These features are 'digital' in that they exist when $x < 1.025$ and disappear when $x \geq 1.025$, while the capacity fade changes smoothly with x.

As now it is clear that overall cycling differences which exist at room and elevated temperatures between the spinel samples are not rooted in structural transformations discussed

above (i.e. two-phase Li de-intercalation, 3.3 and 4.5 V features), the failure mechanism still scales with the average oxidation state and therefore must be linked to either manganese dissolution or the onset of the Jahn–Teller distortion, both of which are dependent on the Mn^{3+} concentration. First let us consider manganese dissolution. From our results presented above in Fig. 22, it is clear that a significant amount of manganese goes into solution at 55 °C. However, for the 'reduced' samples which cycle poorly like the quenched at 800 °C, notice in Fig. 22 that there is no significant difference between manganese evolution from that sample and the one slow cooled at 800 °C. Therefore, the amount of manganese dissolution does not seem to differentiate much from 'oxidized' and 'reduced' samples, with small and large amounts of Mn^{3+}, respectively. Also the relative amounts of manganese which goes into solution should decrease at 22 °C cycling. Therefore, the Jahn–Teller distortion mechanism seems more likely as an explanation for the room-temperature capacity fade. The onset of the Jahn–Teller distortion is brought about by the electronic stabilization of the Mn^{3+} cation by the elimination of the degeneracy of electronic states of the d^4 state. Such stabilization results in the elongation of the MnO_6 symmetry, this elongation results in an overall lattice symmetry conversion from cubic to tetragonal. Therefore, as has been already pointed out by Gummow et al. [14], the offset of the Jahn–Teller distortion and eventual elimination of the structural transformation with increase in x values can be explained by the increase in the Mn^{4+}:Mn^{3+} concentration brought about by an increase in the nominal composition of x in the spinel. This increases the average manganese oxidation state as shown in Fig. 1 and reduces the tendency for the spinel to undergo a Jahn–Teller distortion. Other divalent cations susceptible to substitute for manganese in the octahedral sites can also result in the increase in the average oxidation state of the manganese cation, this is consistent with the improved cycling performance for samples doped with Co or Fe [40–43]. In addition, the Jahn–Teller distortion introduces stress into the structure since it is followed by an increase in unit cell volume and change in c/a ratio. So, the closer to this Jahn–Teller distortion, the larger the amount of internal stress is introduced in the crystal. This crystallite stress could be released upon cycling through the presence of cracks that could spread through the surface of the samples. Such cracks can lead to disconnection of grains and decrease in overall cycling efficiency. Such cracks will also allow a better contact between electrolyte and the spinel surface, a situation which is detrimental to the 55 °C cycling and storage performance.

Although the above discussion discounts manganese dissolution as being the main source of poor cycling performance of the 'reduced' samples both at room temperature and 55 °C, the substantial amount of manganese dissolution shown at 55 °C indicates that dissolution is an intergral part of the overall elevated temperature failure mechanism. The importance of $LiMn_2O_4$ surface area in controlling the degree of capacity fading or self-discharge at 55 °C is clearly tied to

the electrolyte breakdown and manganese dissolution. Thus a legitimate question is, what are the active centers with respect to this electrolyte breakdown/manganese dissolution. Within an $LiMn_2O_4$ particle, the manganese atoms are six-fold coordinated, while the surface manganese (where the crystal terminates) adopts a lower coordination and higher energy. These higher energy manganese ions of lower coordination then act as the active centers towards the electrolyte breakdown/manganese dissolution. If so, surface modification by means of chemical treatments should decrease the $LiMn_2O_4$ particle surface activity. Surface chemistry by means of complexing agents, as will be reported elsewhere [44], have been successfully pursued on these powders in order to passivate these active centers, and thereby to enhance their high-temperature storage performance.

It should be noted that the elevated temperature issue is not only crucial in C/electrolyte/$LiMn_2O_4$ Li-ion cells but can be critical in $LiCoO_2$ or $LiNiO_2$-based Li-ion cells if not operating at elevated temperature under well-defined conditions. In this study we have avoided discussion of the the role of the negative electrode. However, this by no means implies that the negative electrode is transparent to the elevated temperature storage performance of Li-ion cells. For instance, large differences in the storage performance of coke or graphite-based cells have been observed.

5. Conclusions

The results presented here point toward two main mechanisms, manganese dissolution and electrolyte decomposition as the origin of the irreversible self-discharge in the delithiated state and poor storage performance of Li-ion C/electrolyte/$LiMn_2O_4$ cells at 55 °C. Both of these mechanisms scale with the active surface area of the spinel in contact with the electrolyte, therefore reduction of this surface area was found to be critical to the improvement of the elevated temperature performance of the manganese spinel. In the process of coming to a conclusion on the elevated temperature temperature failure mechanisms, we have also investigated the general failure mechanisms which are responsible for the poor cycling of 'reduced' spinels with high initial Mn^{3+} content. In doing so we have discounted the 3.3 V, the 4.5 V feature, and the biphasic Li insertion, extraction as possible origins of the failure. In addition, the 4.0–4.1 V biphasic reaction was proven to be an Li-ordering reaction on the tetrahedral $8a$ sublattice as the distortion was found to disappear at elevated temperatures.

References

[1] T. Nagaura and K. Tazawa, Prog. Batteries Solar Cells, 9 (1990) 20.
[2] K. Ozawa, Solid State Ionics, 69 (1994) 212.
[3] J.R. Dahn, U. Von Sacken, M.R. Jukow and H. Al-Janaby, J. Electrochem. Soc., 138 (1991) 2207.
[4] M.M. Thackeray, P.J. Johnson, L.A. De Picciotto, P.G. Bruce and J.B. Goodenough, Mater. Res. Bull., 19 (1984) 179.
[5] J.M. Tarascon, E. Wang, F.K. Shokoohi, W.R. McKinnon and S. Colson, J. Electrochem. Soc., 138 (1991) 2859.
[6] J.M. Tarascon and D. Guyomard, J. Electrochem. Soc., 138 (1991) 2864.
[7] J.M. Tarascon, D. Guyomard and G.L. Baker, J. Power Sources, 43–44 (1993) 689.
[8] J.M. Tarascon and D. Guyomard, Electrochim. Acta, 38 (1993) 1221.
[9] J.M. Tarascon, US Patent No. 5 196 279 (1993).
[10] D. Guyomard and J.-M. Tarascon, J. Electrochem. Soc., 139 (1992) 937.
[11] J.M. Tarascon, W.R. McKinnon, F. Coowar, T.N. Bowmer, G.G. Amatucci and D. Guyomard, J. Electrochem. Soc., 141 (1994) 1421.
[12] D. Guyomard and J.-M. Tarascon, J. Electrochem. Soc., 140 (1993) 3071.
[13] J.M. Tarascon, US Patent No. 5 425 932 (1995).
[14] R.J. Gummow, A. de Kock and M.M. Thackery, Solid State Ionics, 69 (1994) 59.
[15] D. Guyomard and J.-M. Tarascon, J. Power Sources, 54 (1995) 92.
[16] J.M. Tarascon, F. Coowar, G. Amatuci, F.K. Shokoohi and D. Guyomard, J. Power Sources, 54 (1995) 103.
[17] D. Guyomard and J.M. Tarascon, Solid State Ionics, 69 (1994) 222.
[18] G.G. Amatucci, J.M. Tarascon and L.C. Klein, J. Electrochem. Soc., 143 (1996) 1114.
[19] A.S. Gozdz, C. Schmutz, J.M. Tarascon and P.W. Warren, US Patent No. 5 418 091.
[20] D. Guyomard and J.-M. Tarascon, US Patent No. 5 192 629 (1993).
[21] M.J. Katz, R.C. Clarke and W.F. Nye, Anal. Chem., 28 (1956) 507.
[22] E.J. Cuy, J. Phys. Chem., 25 (1920) 415.
[23] T. Ohzuku, J. Kato, K. Sawai and T. Hirai, J. Electrochem. Soc., 138 (1991) 2556.
[24] A. Yamada, J. Solid State Chem., 122 (1996) 160.
[25] T. Ohzuku, M. Kitagawa and T. Hirai, J. Electrochem. Soc., 140 (1993) 3071.
[26] T. Ohzuku and A. Ueda, J. Electrochem. Soc., 141 (1994) 2972.
[27] M.M. Thacheray, W.I.F. David, P.G. Bruce and J.B. Goodenough, Mater. Res. Bull., 18 (1983) 461.
[28] Y. Gao and J.R. Dahn, Solid State Ionics, 84 (1996) 33.
[29] Y. Gao and J. Dahn, J. Electrochem. Soc., 143 (1996) 1783.
[30] M.M. Thackery, M.F. Mansuetto, D.W. Dees and D.R. Vissers, Mater. Res. Bull., 21 (1996) 133.
[31] D.W. Murphy, F.J. DiSalvo, J.N. Carides and J.V. Waszczak, Mater. Res. Bull., 13 (1978) 1395.
[32] W.I.F. David, M.M. Thakery, P.G. Bruce and J.B. Goodenough, Mater. Res. Bull., 19 (1984) 99.
[33] G. Pistoia and G. Wang, Solid State Ionics, 66 (1993) 135.
[34] Y. Xia and M. Yoshio, J. Electrochem. Soc., 143 (1996) 825.
[35] G.G. Amatucci et al., to be published.
[36] J.N. Reimers and J.R. Dahn, J. Electrochem. Soc., 139 (1992) 2091.
[37] Y. Gao, K. Myrtle, M. Zheng, J.N. Reimers and J. Dahn, Phys. Rev. B., submitted for publication.

[38] N. Sugeno, *US Patent No. 5 168 019* (1991).

[39] G.G. Amatucci, J.M. Tarascon, C. Schmutz, D. Larcher, T. Gozdz and F. Shokoohi, *189th Meet The Electrochemical Society, Los Angeles, CA, USA, Spring 1996*.

[40] J.L. Baudour, F. Bouree, M.A. Fremy, R. Legros, A. Rousset and B. Gillot, *Phys. B, 97* (1992) 180.

[41] Y. Toyoguchi, *Eur. Patent No. 0 390 085* (1990).

[42] R.J. Gummow, A. de Kock and M.M. Thackeray, *J. Electrochem. Soc.*, *69* (1994) 59.

[43] R. Bittihn, R. Herr and D. Hoge, *J. Power Sources, 43–44* (1993) 233.

[44] G.G. Amatucci et al., to be published.